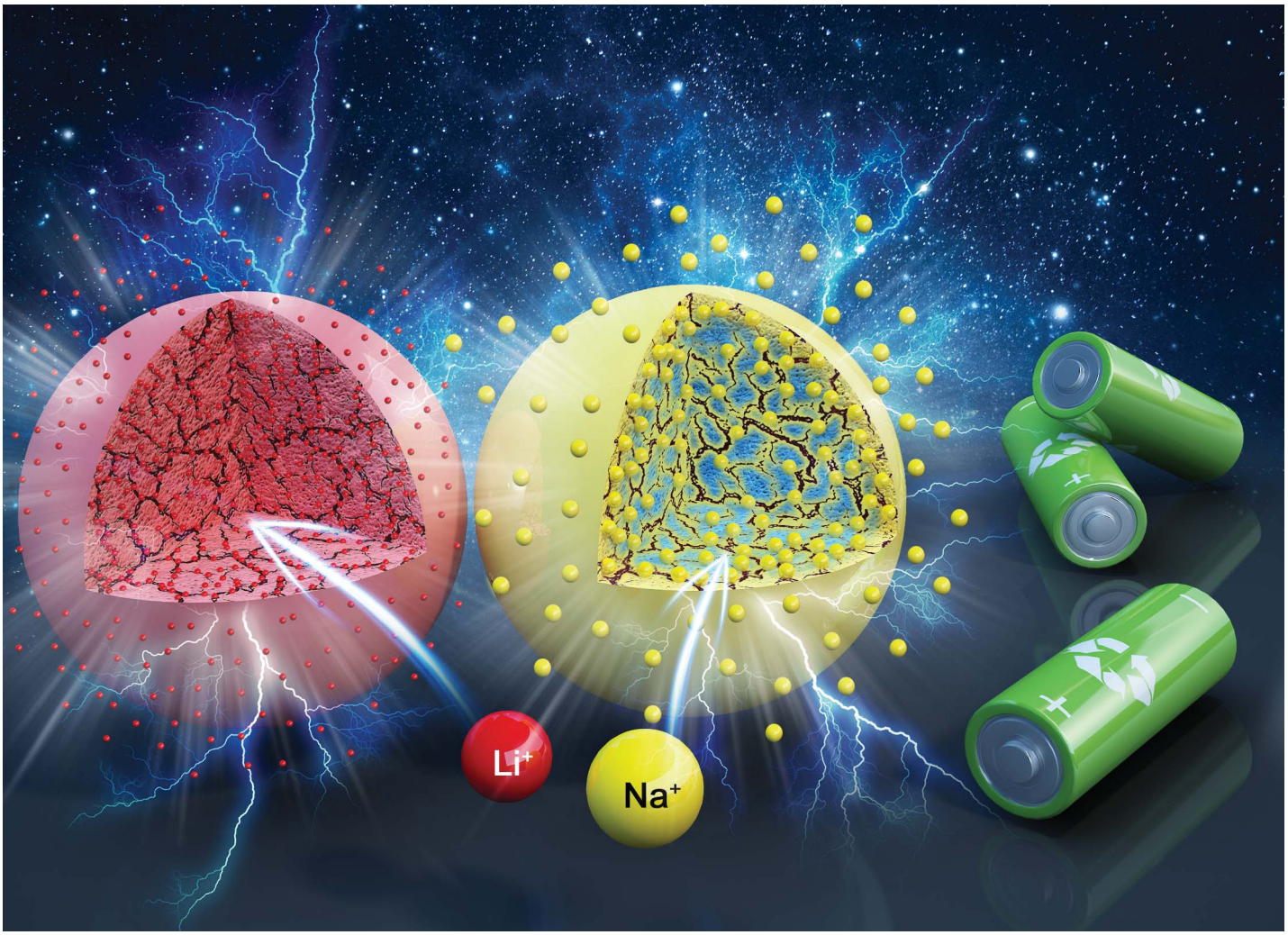

An article showcasing research on Li-ion and Na-ion transportation and storage properties in various sized TiO_2 spheres by Yong Li and Prof. Yan-Bing He, Graduate School at Shenzhen, Tsinghua University, China.

Li-ion and Na-ion transportation and storage properties in various sized TiO_2 spheres with hierarchical pores and high tap density

Size-controlled TiO_2 spheres with hierarchically porous architectures and high tap density are crafted by a facile hydrolysis route. The pore distribution and size of the TiO_2 spheres are found to exert profound influence on Li-ion and Na-ion storage and transportation.

As featured in:

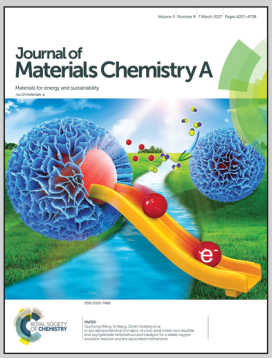

See Yan-Bing He, Baohua Li *et al.*, *J. Mater. Chem. A*, 2017, **5**, 4359.

ROYAL SOCIETY OF CHEMISTRY

rsc.li/materials-a

Registered charity number: 207890

Journal of Materials Chemistry A

PAPER

View Article Online
View Journal | View Issue

CrossMark click for updates

Cite this: J. Mater. Chem. A, 2017, 5, 4359

Li-ion and Na-ion transportation and storage properties in various sized TiO_2 spheres with hierarchical pores and high tap density†

Yong Li,‡[ab] Shuan Wang,‡[a] Yan-Bing He,*[a] Linkai Tang,[ab] Yusuf Valentino Kaneti,[a] Wei Lv,[a] Zhiqun Lin,[c] Baohua Li,*[a] Quan-Hong Yang[a] and Feiyu Kang[ab]

Received 4th October 2016
Accepted 9th November 2016

DOI: 10.1039/c6ta08611j

www.rsc.org/MaterialsA

Titanium oxide (TiO_2) has attracted great interest as a promising anode material for lithium (Li) ion batteries (LIBs) and sodium (Na) ion batteries (SIBs). However, the key factors that dictate the Li-ion and Na-ion storage and transportation in TiO_2 remain unclear. Herein, we report a facile hydrolysis route to crafting a variety of high tap-density TiO_2 spheres with controllable size and hierarchical pores. The Li-ion and Na-ion storage properties based on these TiO_2 spheres were systematically investigated. The pore distribution and the size of TiO_2 spheres were found to exert profound influence on the Li-ion and Na-ion storage and transportation. The Li-ion storage and transportation in dense TiO_2 spheres was dependent mainly upon the micropore distribution and volume and independent of the size of spheres. In contrast, the excellent Na-ion storage and transportation in TiO_2 spheres was enabled by the loose structure with a large macroscopic pore volume and shortened Na-ion diffusion length. High tap-density TiO_2 spheres (1.06 g cm^{-3}) with superior Li-ion and Na-ion storage properties were produced, exhibiting a Li-ion storage specific capacity of 189 mA h g^{-1} at 1C and a high capacity retention of 88.1% after 100 cycles, and a Na-ion storage specific capacity of 184 mA h g^{-1} at 1C and capacity retention of 90.5% after 200 cycles. The ability to understand the critical factors controlling the Li-ion and Na-ion storage in high tap-density TiO_2 spheres enables their implementation for practical applications in Li-ion and Na-ion batteries.

Published on 14 November 2016. Downloaded on 04/04/2017 19:02:09.

Introduction

Titanium oxide (TiO_2) has garnered much attention as a promising anode material for lithium ion batteries (LIBs) due to its abundance, non-toxicity, low cost and stable chemical properties.[1–4] Recently, various polymorphs of TiO_2 such as rutile,[5–7] anatase[8–12] and TiO_2 (B)[1,13] with high lithium storage properties have been widely studied as anode materials for LIBs. Anatase TiO_2 has a high lithium ion insertion/extraction potential at 1.7 V (*vs.* Li^+/Li), which is inherently safe due to the absence of Li-dendrite electroplating.[14] Furthermore, the low volume change (less than 4%) and high structural stability of anatase TiO_2 during the charge/discharge process can lead to a prolonged cycling life.

In addition to LIBs, TiO_2 nanomaterials have also been investigated as anode materials for SIBs.[15,16] Different from LIBs, the charge/discharge mechanism of SIBs involves the partial reduction of TiO_2 by Na ions and the formation of metallic titanium, sodium oxide, and amorphous sodium titanate, as well as insertion of Na ions into the TiO_2 lattice.[17] Notably, development of TiO_2 that can be applied for both Li-ion and Na-ion batteries has recently received much interest.[18–21] For instance, Iversen *et al.* synthesized TiO_2 (B)/anatase mixtures by a hydrothermal method and evaluated their electrochemical performance in Li-ion and Na-ion coin cells. Although the mixtures exhibit good Li-ion storage properties, the Na-ion storage properties still require further improvement.[18] Clearly, investigation into the difference in Li-ion and Na-ion storage properties due to the use of TiO_2 with varied architectures may improve the understanding of the Na-ion storage mechanism and expand the application of TiO_2 as an anode material.

It is notable that the poor ionic and electronic conductivities of TiO_2 anode materials pose great challenges in satisfying the requirements of high energy-density batteries. To date, different strategies have been developed to enhance the ionic and

[a]Engineering Laboratory for the Next Generation Power and Energy Storage Batteries, Graduate School at Shenzhen, Tsinghua University, Shenzhen, 518055, PR China. E-mail: he.yanbing@sz.tsinghua.edu.cn; libh@mail.sz.tsinghua.edu.cn

[b]Laboratory of Advanced Materials, Department of Materials Science and Engineering, Tsinghua University, Beijing, 100084, PR China

[c]School of Materials Science and Engineering, Georgia Institute of Technology Atlanta, GA 30332, USA

† Electronic supplementary information (ESI) available: SEM images of amorphous TiO_2 spheres; XPS spectra of TiO_2 spheres; Raman spectrum of graphene oxide; TGA curves of TiO_2 spheres; electrochemical properties of the TiO_2 (1 : 4) electrode with and without the addition of GO; comparison of the electrochemical properties of the TiO_2 electrodes between this work and other literature reports. See DOI: 10.1039/c6ta08611j

‡ These authors contributed equally to this work.

Published on 14 November 2016. Downloaded on 04/04/2017 19:02:09.

electronic conductivities of TiO_2, including the fabrication of shape-controlled nanomaterials (*e.g.*, nanosheets, nanowires, nanospheres), porous structures, carbon coating and hybridization with graphene and metal powders.[14,22–25] However, the produced nanomaterials or porous nanostructures usually exhibit low tap density which results in low volumetric energy density.[1] TiO_2 microspheres assembled using nanoparticles by the hydrothermal method have been investigated for LIBs[3] and SIBs.[26] However, the hydrothermal strategies involve high energy consumption, which is unfavourable for mass production. Clearly, it is highly desirable to develop an efficient preparative strategy to produce hierarchical porous TiO_2 spheres composed of small nanograins with high tap density for achieving high rate performance and large volumetric energy density for TiO_2 anode-based Li-ion and Na-ion storage. The hierarchical porous structure of TiO_2 often greatly improves its ionic conductivity and interfacial storage of Li and Na ions. In addition, reduced graphene oxide (rGO) can also be combined with TiO_2 to enhance its electronic conductivity and mechanical properties for Li-ion and Na-ion storage.[27,28] However, the introduction of high rGO content (more than 10%) with a large surface area ($\sim$200–300 $m^2 g^{-1}$) often leads to a low volumetric energy density of TiO_2.[1,10,11,15,29] Therefore, it is important to develop a TiO_2 anode material combining the high tap density with the enhanced electrochemical properties. It is well known that pore size and distribution have considerable influence on the tap density of anode materials. However, the key factors that influence the Li-ion and Na-ion storage in TiO_2, particularly the effects of pore distribution and particle size of TiO_2, are still not well understood.

Herein, we report a facile low-temperature hydrolysis route to crafting size-controlled TiO_2 spheres composed of densely assembled nanocrystals and decorated by a trace amount of rGO. The as-prepared TiO_2 spheres exhibited hierarchical porous architecture containing micro-, meso-, and macropores with tunable sizes ranging from 100 nm to 1.5 μm. The pore distribution and the size of TiO_2 spheres were found to play different roles in governing the Li-ion and Na-ion storage and transportation. Interestingly, the Li-ion storage and transportation were dependent upon the distribution and volume of micropores but independent of the size of spheres. In sharp contrast, the decrease in the size of TiO_2 spheres was demonstrated to reduce the accumulation of TiO_2 nanocrystals and increased the pore volume to shorten the Na-ion diffusion and penetration length, and thus achieving high-performance for Na-ion storage. The reaction rate for Na-ion storage was largely determined by the diffusion and penetration length of Na-ions. The as-prepared TiO_2 spheres displayed excellent Li-ion and Na-ion storage properties, and a high tap density of 1.06 g cm^{-3}, which is considerably higher than those of commercial TiO_2 anodes (0.108 g cm^{-3}) and mesoporous TiO_2 with the highest reported packing density (0.714 g cm^{-3}).[14,30]

Experimental section

Synthesis of TiO_2 spheres

TiO_2 spheres were prepared by a viable hydrolysis approach at low temperature. Graphene oxide was synthesized *via* a modified Hummers method as previously reported.[31] In a typical procedure, graphene oxide (GO) aqueous solution was firstly prepared *via* the ultrasonication of graphite oxide for 2 h. In a general way, 0.5 g of TiN nanopowders (Aladdin, 20 nm), 68 mL of H_2O, 16 mL of the GO aqueous solution (2 mg mL^{-1}), 16 mL of 30% H_2O_2 (Sinopharm Chemical Reagent Co., Ltd), and 6 mL of 25% $NH_3 \cdot H_2O$ (Sinopharm Chemical Reagent Co., Ltd) were added into a beaker and stirred for 20 min to obtain the precursor solution. Subsequently, 53 mL, 106 mL, 212 mL and 424 mL of absolute ethanol (Sinopharm Chemical Reagent Co., Ltd) were added into each precursor solution to yield four solutions with different ratios of the precursor to absolute ethanol (2 : 1, 1 : 1, 1 : 2 and 1 : 4, respectively). The solutions were then dried in an oven at 80 °C, yielding a grey powder of amorphous TiO_2 spheres. Finally, the black powders were further annealed in an Ar atmosphere at 450 °C at a heating rate of 5 °C min^{-1} for 3 h to form anatase TiO_2 spheres (denoted as TiO_2 (2 : 1), TiO_2 (1 : 1), TiO_2 (1 : 2) and TiO_2 (1 : 4), respectively, depending on the content of absolute ethanol added).

Characterization

Scanning electron microscope (SEM) imaging of TiO_2 spheres was performed using a field emission scanning electron microscope (ZEISS Supra55) at 20 kV. Transmission electron microscope (TEM) images were collected using a high-resolution transmission electron microscope (HRTEM, FEI TECNAI G2 F30) at an accelerating voltage of 300 kV. X-ray diffraction (XRD) patterns were obtained using a Rigaku D/MAX 2500/PC diffractometer using Cu-K_α radiation (λ = 0.154 nm). Raman spectra were recorded using a HORIBA Jobin Yvon LabRAM HR800 with 532 nm laser excitation. XPS spectra were obtained using an ESCALAB 250Xi. Thermogravimetric analysis (TGA) was conducted with a NETZSCH STA 449F3 at a heating rate of 10 °C min^{-1} from room temperature to 800 °C in air. Nitrogen adsorption/desorption isotherms were obtained using an automated adsorption apparatus (Micromeritics ASAP 2020).

Electrochemical measurements

Electrochemical measurements of TiO_2 for Li-ion and Na-ion storage were performed using CR2032 half cells. The cathode was composed of as-prepared TiO_2 spheres, acetylene black and polyvinylidene fluoride (PVDF) with an 80 : 10 : 10 weight ratio. For Li-ion cells, Li foil was used as the anode, a microporous polypropylene film (Celgard 2500, Celgard Inc., USA) was used as the separator, and 1 M $LiPF_6$ in a mixture of ethylene carbonate (EC) and dimethyl carbonate (DMC) (volume ratio = 1 : 1) was used as the electrolyte. Similarly, for Na-ion cells, Na foil was used as the anode with a glass microfiber filter (Whatman, grade GF/B) with a pore size of 1 μm as the separator and 1 M $NaPF_6$ in a mixture of ethylene carbonate (EC) and diethyl carbonate (DEC) (volume ratio = 1 : 1) as the electrolyte. Both Li-ion and Na-ion cells were assembled in an argon-filled glove box and galvanostatically cycled (1–3 V for Li-ion battery, 0.02–3 V for Na-ion battery) on a multichannel battery tester (LAND 2001A Battery Testing System). The electrochemical impedance spectra (EIS) were obtained by applying

 This journal is © The Royal Society of Chemistry 2017

Published on 14 November 2016. Downloaded on 04/04/2017 19:02:09.

a perturbation voltage of 5 mV over a frequency range from 100 kHz to 10 mHz using a VMP3 multichannel electrochemical station. Cyclic voltammograms (CVs) were recorded using the VMP3 multichannel electrochemical station and MACCOR at a scan rate of 0.1 mV s^{-1} in the range of 1.0–3.0 V and 0.02–3.0 V for LIBs and SIBs, respectively.

Results and discussion

Synthesis mechanism of TiO_2 spheres

The precursors TiO_2 spheres were synthesized *via* a facile hydrolysis process in a water–ethanol solution at 80 °C. Amorphous TiO_2 spheres were formed after the hydrolysis reaction (Fig. S1†), which were subsequently annealed in an Ar atmosphere at 450 °C to yield crystalline TiO_2 spheres. By adjusting the volume ratios of the precursor solution consisting of GO, H_2O_2 and $NH_3 \cdot H_2O$ to absolute ethanol (*i.e.*, precursor : absolute ethanol = 2 : 1, 1 : 1, 1 : 2 and 1 : 4), four different types of TiO_2 spheres with distinct morphology and particle size were obtained (denoted as TiO_2 (2 : 1), TiO_2 (1 : 1), TiO_2 (1 : 2), TiO_2 (1 : 4)) (Fig. 1 and 2). Fig. 2 depicts the formation process of TiO_2 spheres. First, the TiN nanopowders were dissolved in deionized water with the assistance of H_2O_2 and $NH_3 \cdot H_2O$ to form Ti^{4+}, which was rapidly transformed to a Ti–peroxo complex $[Ti(OH)_3O_2]^-$ that is highly soluble in water yet hardly soluble in ethanol.[32–34] Small amorphous TiO_2 nanoparticles were formed, and their size gradually increased after the addition of a certain amount of ethanol.[35] Finally, the small TiO_2 nanoparticles were assembled together to produce amorphous TiO_2 spheres. The size of TiO_2 spheres was determined by the amount of added ethanol.

The morphology of the as-prepared TiO_2 spheres was characterized by scanning electron microscopy (SEM) (Fig. 1). The TiO_2 spheres have a dense structure. The size of TiO_2 spheres depends strongly on the volume ratio of the precursor solution to ethanol. The TiO_2 spheres do not exhibit a perfect spherical morphology, which may be attributed to the presence of GO

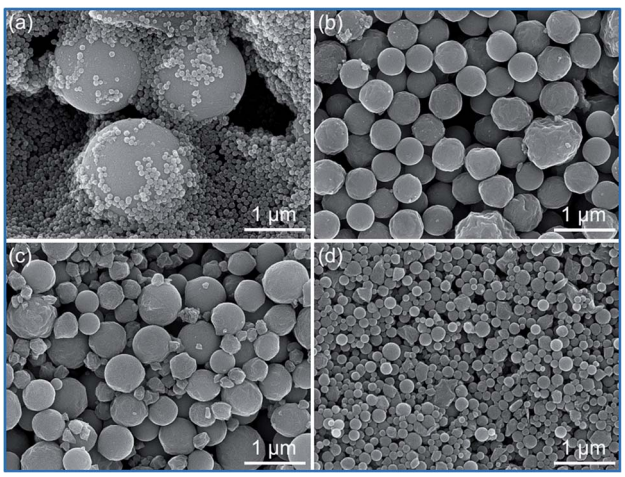

Fig. 1 SEM images of the four TiO_2 spheres: (a) TiO_2 (2 : 1), (b) TiO_2 (1 : 1), (c) TiO_2 (1 : 2) and (d) TiO_2 (1 : 4). The ratios of the precursor to absolute alcohol in each TiO_2 sphere are shown in parentheses.

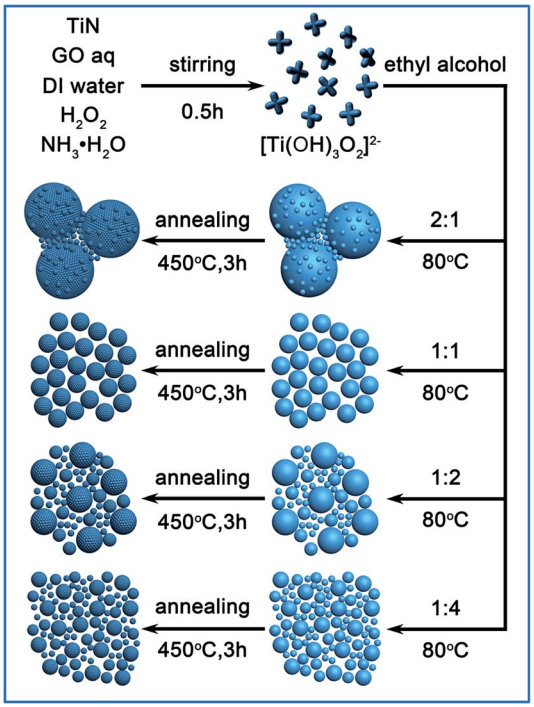

Fig. 2 Schematic illustration of the synthesis of four TiO_2 spheres with different sizes by adjusting the volume ratios of the precursor solution consisting of GO, H_2O_2 and $NH_3 \cdot H_2O$ to absolute ethanol.

during the growth of TiO_2 spheres. The diameter of TiO_2 spheres can be easily tuned from the nanoscale to microscale by adjusting the volume ratio of the precursor solution to ethanol. The average diameter of TiO_2 spheres gradually decreases from *ca.* 1.5 μm to 100 nm as the volume ratio of the precursor solution to ethanol decreases from 2 : 1, 1 : 1, 1 : 2 to 1 : 4. The TiO_2 (2 : 1) sample contains a few microspheres surrounded by a large number of nanospheres with an average diameter of 90 nm (Fig. 1a), while the TiO_2 (1 : 1) sample consists of microspheres with a uniform size of *ca.* 500 nm (Fig. 1b). As the precursor solution to ethanol volume ratio changes to 1 : 2 (*i.e.*, the TiO_2 (1 : 2) sample), sub-micron sized spheres with the sizes ranging from *ca.* 200 nm to 700 nm (an average size of *ca.* 500 nm) are obtained (Fig. 1c). The average size of the TiO_2 (1 : 4) spheres further decreases to approximately 100–150 nm (Fig. 1d). As ethanol is added to the aqueous precursor solution, the metastable $Ti(OH)_4$ formed by the hydrolysis of the titanium peroxide complex is further condensed into primary amorphous TiO_2 particles, which gradually nucleate and grow into TiO_2 spheres with different sizes during the heating process at 80 °C. The addition amount of ethanol influences the concentration of $Ti(OH)_4$ that determines the nucleation and growth rates of amorphous TiO_2 particles and results in the formation of TiO_2 spheres with different sizes.

Characteristics of TiO_2 spheres

The XRD patterns of the four different types of TiO_2 spheres were examined to identify their crystallographic structures. As shown in Fig. 3a, the XRD reflections of all four samples are

Published on 14 November 2016. Downloaded on 04/04/2017 19:02:09.

consistent with JCPDS card no. 21-1272 and can be well-indexed to anatase TiO_2. The diffraction intensities remain almost unchanged with variation in the amount of ethanol. According to the Debye–Scherrer equation (Table 1), the primary TiO_2 particle size slightly changes with the change of the ratio of precursor solution to ethanol. The XPS analysis shows that the C 1s XPS spectrum of the four samples contains a very small peak of O–C=O (288.7 eV) (Fig. S2†), suggesting that the GO has been converted to rGO during the thermal annealing process at 450 °C.[24] The binding energies at 459.0 eV and 464.8 eV assigned to Ti $2p_{3/2}$ and Ti $2p_{1/2}$ confirmed the Ti^{4+} in TiO_2,[36] suggesting that the final TiO_2 spheres do not contain Ti^{3+} and oxygen vacancies. In addition, the small N 1s XPS peak at 400.1 eV indicates that a low N content (<2%) in a similar state exists in all four TiO_2 spheres, which may be ascribed to the hydrolysis products of TiN that are located within the TiO_2 spheres.[36] The results described above indicate that the Li-ion and Na-ion storage performance of TiO_2 spheres is not affected by the N species and oxygen vacancies, but by their particle sizes and structures.

In order to confirm the chemical composition of TiO_2 spheres, Raman measurements were performed (Fig. 3b). The peaks at 143, 195, 400, 516, and 639 cm^{-1} are assigned to E_g, E_g, B_{1g}, A_{1g} and E_g, respectively, corresponding to the different characteristic vibration modes of anatase TiO_2.[37,38] The existence of these peaks suggests that the crystalline states of TiO_2 (2 : 1), TiO_2 (1 : 1), TiO_2 (1 : 2) and TiO_2 (1 : 4) samples are similar. In addition, two main bands are observed at around 1350 cm^{-1} and 1580 cm^{-1}, corresponding to the D-band and G-band of carbon, respectively.[39] The D-peak suggests the disruption of the symmetrical hexagonal graphitic lattice associated with the internal structure. The G-peak indicates the in-plane stretching motion of a symmetric sp^2 C–C bond.[40,41] The value I_D/I_G (the peak intensity ratio) can be used to evaluate the degree of graphitic carbon structure. The I_D/I_G values of the four TiO_2 samples (Table 1) are almost equal to that of GO annealed at 450 °C (1.87) in Fig. S3.† According to the thermogravimetric analysis (TGA) measurements, the contents of rGO in TiO_2 (2 : 1), TiO_2 (1 : 1), TiO_2 (1 : 2) and TiO_2 (1 : 4) are 1.0 wt%, 1.2 wt%, 0.4 wt% and 1.2 wt%, respectively (Fig. S4†). The incorporation of rGO into TiO_2 spheres can provide a high-speed conductive network for the transportation of electrons.[42,43]

The porosity of TiO_2 spheres was characterized using nitrogen (N_2) adsorption–desorption isotherms. As shown in Fig. 3c, all four samples show typical type-IV nitrogen adsorption–desorption isotherms with a clear H3 hysteresis loop, indicating the presence of mesopores.[44] The Brunauer–Emmett–Teller (BET) surface areas of samples TiO_2 (2 : 1), TiO_2 (1 : 1), TiO_2 (1 : 2), and TiO_2 (1 : 4) are calculated to be 95.0, 102.1, 102.5 and 93.4 $m^2\ g^{-1}$, respectively (Table 1). The Barrett–Joyner–Halenda (BJH) pore volume and pore size distribution were calculated from the adsorption branches of the isotherms (Fig. 3d). The TiO_2 (2 : 1) sample has the largest pore volume (0.33 $cm^3\ g^{-1}$), which may be attributed to the coexistence of microspheres and nanospheres with markedly different sizes. All samples have micropores (<2 nm) and mesopores (centered at 5.5 nm), which can be attributed to the inter-grain packing in the TiO_2 polycrystalline structure. Notably, the TiO_2 (2 : 1) and TiO_2 (1 : 4) samples also possess a broad range of macropores from 50 nm to 100 nm derived from the accumulation of different sized spheres because some relatively large and irregular particles exist in the TiO_2 (2 : 1) and TiO_2 (1 : 4). Such hierarchical pore distributions containing macropores, mesopores and micropores may lead to different Li-ion and Na-ion transportation and storage properties. The existence of micropores enables a high specific surface area which is beneficial for providing a sufficient interfacial area between the electrode and electrolyte, while the presence of meso- and macropores promotes efficient mass transport of the electrolyte throughout the electrode.[45]

In order to further understand the internal fine structure of TiO_2 spheres, the morphologies of the TiO_2 (2 : 1), TiO_2 (1 : 1), TiO_2 (1 : 2) and TiO_2 (1 : 4) spheres were examined by TEM

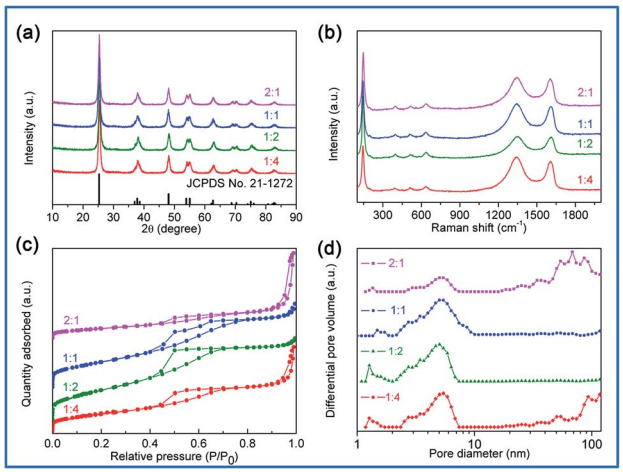

Fig. 3 (a) XRD patterns, (b) Raman spectra, (C) N_2 adsorption/desorption plots and (d) pore size distributions of TiO_2 spheres.

Table 1 Summary of surface area, pore volume, grain size, value of I_D/I_G, tap density, Warburg factor (σ_{Li}, σ_{Na}) and lithium ion diffusion coefficient (D_{Li}) of TiO_2 spheres with different sizes

Samples	Surface area ($m^2\ g^{-1}$)	Pore volume ($cm^3\ g^{-1}$)	Grain size (nm)	I_D/I_G	ρ_{Li} ($g\ cm^{-3}$)	σ_{Li}	D_{Li} ($cm^2\ s^{-1}$)	σ_{Na}
TiO_2 (2 : 1)	95.0	0.33	17.1	1.87	0.90	3.00	1.89×10^{-13}	176.9
TiO_2 (1 : 1)	102.1	0.14	15.9	1.29	1.18	6.24	2.22×10^{-14}	230.7
TiO_2 (1 : 2)	102.5	0.11	17.5	1.57	1.25	2.25	1.51×10^{-13}	196.7
TiO_2 (1 : 4)	93.4	0.18	18.3	1.64	1.06	2.09	2.91×10^{-13}	53.7

This journal is © The Royal Society of Chemistry 2017

Published on 14 November 2016. Downloaded on 04/04/2017 19:02:09.

(Fig. 4). All the samples exhibit a well-defined crystalline structure with a lattice spacing of 0.351 nm, which is consistent with the (101) facet of anatase TiO_2 (Fig. 4b, d, f and g). It is worth noting that the HRTEM images of these samples revealed the polycrystalline porous structures composed of the interconnected primary crystalline particles. The smaller sized TiO_2 (2 : 1) and TiO_2 (1 : 4) spheres possess a relatively highly porous structure compared to the larger sized TiO_2 (1 : 1) and TiO_2 (1 : 2) spheres. In particular, the TiO_2 (1 : 1) sample displays a highly dense structure in comparison to other samples, which may retard the Li-ion and Na-ion transportation. Although the TiO_2 (1 : 2) sample shows less dense packing than the TiO_2 (1 : 1) sample, most of the interior area of TiO_2 (1 : 2) spheres is densely formed by several TiO_2 nanocrystals. Owing to the interconnected crystalline particles of the TiO_2 (1 : 2) and the TiO_2 (1 : 1) samples with dense structures and large sizes, their tap densities are as high as 1.25 g cm^{-3} and 1.18 g cm^{-3}, respectively, which are much larger than that of the TiO_2 (2 : 1) and TiO_2 (1 : 4) samples (0.90 g cm^{-3} and 1.06 g cm^{-3}, respectively) with a high fraction of tiny TiO_2 spheres (Table 1). The TiO_2 (1 : 2) sample containing 550 nm and 100 nm spheres achieves the highest tap density due to the dense packing of the different sized spheres. We note that all as-prepared TiO_2 spheres have much higher tap densities than commercial TiO_2 anodes (0.108 g cm^{-3}) and mesoporous TiO_2 (0.714 g cm^{-3}).[15,30] The high tap density of as-prepared TiO_2 spheres is beneficial for developing lithium ion power batteries with high volumetric energy density.

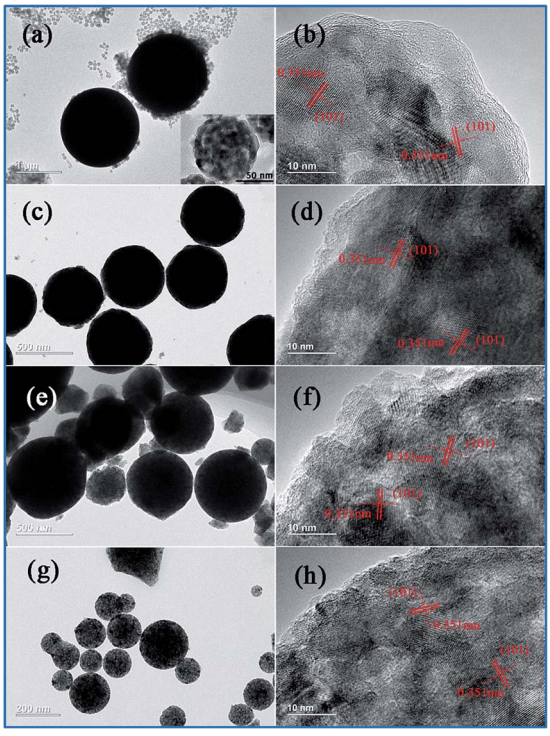

Fig. 4 TEM and HRTEM images of the TiO_2 spheres obtained with different precursor solution–ethanol ratios: (a and b) TiO_2 (2 : 1), (c and d) TiO_2 (1 : 1), (e and f) TiO_2 (1 : 2), and (g and h) TiO_2 (1 : 4).

Electrochemical performance of TiO_2 spheres

The electrochemical properties of the as-prepared TiO_2 spheres as anode materials in LIBs were evaluated by constructing the half cells (see Experimental section) (Fig. 5). Fig. 5a shows the rate and cycling performances of the TiO_2 spheres electrode at various discharge rates. The discharge/charge curves of the four TiO_2 spheres at a current density of 0.1C show two well-defined voltage plateaus at 1.77 V and 1.88 V (Fig. 5b). The TiO_2 (2 : 1), TiO_2 (1 : 1), TiO_2 (1 : 2) and TiO_2 (1 : 4) electrodes have discharge capacities of 181.9, 182.5, 197.7 and 216.9 mA h g^{-1} at 0.5C (1C = 168 mA g^{-1}), respectively. Among the four types of TiO_2 spheres, the TiO_2 (1 : 4) electrode exhibits the best electrochemical performance with the discharge capacities of 216.9, 189.1, 167, 136.4 and 101.7 mA h g^{-1} at 0.5C, 1C, 2C, 5C and 10C, respectively. When the current density returns to 0.5C after the rate cycling test, a discharge capacity of 185.7 mA h g^{-1} is obtained. The cycle performance was then further tested on the same cell by (dis)charging for 100 cycles at 1C. The reversible capacity is 169 mA h g^{-1} and the capacity retention is 88.1% after 100 cycles.

It is noteworthy that the rate performance of the TiO_2 (1 : 2) electrode is only slightly lower than that of the TiO_2 (1 : 4) electrode, whereas the TiO_2 (1 : 1) electrode shows the lowest rate performance despite its relatively uniform size distribution. As shown in Fig. 1d, the TiO_2 (1 : 4) sample has the smallest size with a relatively uniform size distribution, and similar appearance of micropores to the TiO_2 (1 : 2) sample. However, the volume of micropores of the TiO_2 (2 : 1) and TiO_2 (1 : 1) samples is obviously less than that of the TiO_2 (1 : 4) and TiO_2 (1 : 2) samples, suggesting that the Li-ion storage and transportation in TiO_2 spheres depend primarily on the micropore distribution and volume. The existence of micropores is advantageous in providing sufficient transport of Li-ions inside the TiO_2 spheres to achieve a high speed lithiation reaction. Furthermore, the larger interface between the micropores and electrolyte offers additional sites for Li-ion storage, which is beneficial for enhancing the specific capacity at high current densities. The poor rate performance of the TiO_2 (1 : 1) electrode suggests that the highly compact structure with micropores restricts the lithium ion diffusion during the high rate charge/discharge process. The good rate performance of the TiO_2 (1 : 2) electrode indicates that the lithium ion can easily reach the centre of the interior dense area of TiO_2 (1 : 2) spheres formed by several TiO_2 nanocrystals through micropores. The electrochemical properties of pure TiO_2 spheres without the rGO modification were also tested for comparison, as shown in Fig. S5.† Clearly, the electrochemical properties of TiO_2 spheres for LIBs have been significantly improved by the modification with rGO due to the enhanced electrical conductivity. Furthermore, the rGO-modified TiO_2 spheres exhibit better electrochemical performance for LIBs than other TiO_2-based anode materials reported in previous studies (Table S1†).[1,3,4,8,10,24,46–49]

Cyclic voltammetry (CV) characteristics of the four TiO_2 electrodes were measured at a scan rate of 0.1 mV s^{-1} in the range of 1.0–3.0 V to clarify the kinetic behavior of the annealed TiO_2 spheres (Fig. 5c). The cathodic/anodic peaks located at

Published on 14 November 2016. Downloaded on 04/04/2017 19:02:09.

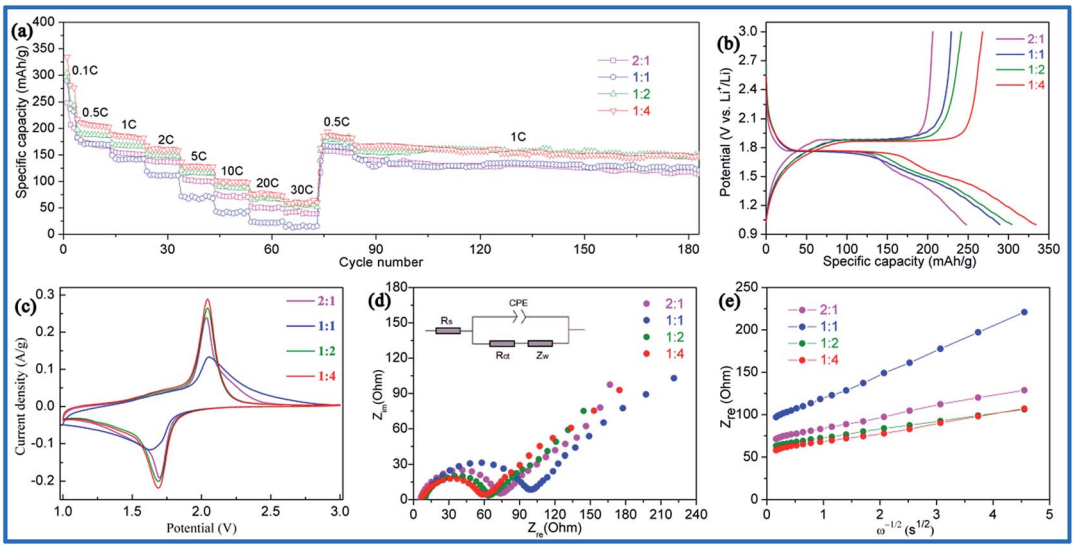

Fig. 5 Electrochemical characterization of TiO_2 spheres for LIBs: (a) the rate and cycling performances, (b) the first charge/discharge curves, (c) the cyclic voltammetry (CV) curves, (d) the Nyquist plots and (e) the plot of Z_{re} *versus* $\omega^{-1/2}$ in the low-frequency region.

1.69 V and 2.04 V are associated with the insertion/extraction of lithium ion in the anatase TiO_2 lattice. The voltage gap between the anodic and cathodic peaks (ΔE_p) of the TiO_2 (2 : 1), TiO_2 (1 : 2) and TiO_2 (1 : 4) electrodes is about 0.35 V, which is obviously smaller than 0.42 V for the TiO_2 (1 : 1) electrode. In addition, the peak current density of the TiO_2 (1 : 4) electrode is the highest among the four TiO_2 electrodes, which is slightly larger than that of the TiO_2 (1 : 2) electrode but much larger than that of the TiO_2 (1 : 1) electrode, reflecting the good kinetic behavior of the TiO_2 (1 : 4) and TiO_2 (1 : 2) electrodes, and poor kinetic property of the TiO_2 (1 : 1) electrode. The electrochemical impedance spectra (EIS) of the four TiO_2 electrodes were also obtained in the discharge platform after 5 cycles at 0.1C, which were simulated by the Z-view software using the equivalent circuit models. Nyquist plots of the TiO_2 spheres display a depressed semicircle in the moderate frequency region and a straight line in the low-frequency region (Fig. 5d), which are related to a charge transfer process and a Warburg diffusion process, respectively. The TiO_2 (1 : 4) electrode exhibits a lower charge transfer resistance (R_{ct}, 51.3 ohms) than the TiO_2 (2 : 1), TiO_2 (1 : 1) and TiO_2 (1 : 2) electrodes (64.4, 84.8 and 53.3 ohms, respectively). In addition, the lithium ion diffusion coefficients (D_{Li}) of the TiO_2 (1 : 4), TiO_2 (1 : 2) and TiO_2 (2 : 1) electrodes are 2.91×10^{-13}, 1.51×10^{-13} and 1.89×10^{-13} cm^2 s^{-1}, respectively, which are one order magnitude larger than that of the TiO_2 (1 : 1) electrode (2.22×10^{-14} cm^2 s^{-1}), signifying that the smaller sized particles and micropores of the electrode materials have a synergistic effect for the lithium ion diffusion (Fig. 5e and Table 1). The much lower R_{ct} and higher D_{Li} of the TiO_2 (1 : 4) electrode contribute to its outstanding rate performance and cycling life.

Similarly, the electrochemical properties of as-prepared TiO_2 spheres as anode materials in SIBs were also evaluated using half cells (see Experimental section), as shown in Fig. 6. Fig. 6a shows the rate performance of the TiO_2 sphere electrodes at various discharge rates. The TiO_2 (2 : 1), TiO_2 (1 : 1), TiO_2 (1 : 2) and TiO_2 (1 : 4) electrodes can achieve discharge capacities of 212.2, 77.9, 120.2, and 233.1 mA h g^{-1}, respectively (Fig. 6b). Similar to the performance in LIBs, the TiO_2 (1 : 4) electrode also presents the best performance in SIBs among the four TiO_2 electrodes. Its discharge capacities at 0.2C, 0.5C, 1C, 2C and 5C (1C = 168 mA g^{-1}) are 200.8, 180, 164.8, 143 and 88 mA h g^{-1}, respectively. After a total of 60 cycles, the current density returns to 0.1C and a discharge capacity of 206.9 mA h g^{-1} is obtained. The capacity retention of the electrode is 90.5% after 200 cycles at 1C (Fig. 6c). To the best of our knowledge, this performance of SIBs is among the highest reported performance for TiO_2 nanostructures (Table S2†).[17,18,20,26,50–55] Interestingly, the performance of the SIB using the TiO_2 (2 : 1) electrode is obviously better than that of the TiO_2 (1 : 2) electrode, indicating the difference in their Na-ion and Li-ion storage properties. The high Na-ion storage performance of the TiO_2 (2 : 1) and TiO_2 (1 : 4) electrodes may be attributed to a large fraction of very small nanospheres with relatively loose structures and broad macropores due to the accumulation of different nanospheres, which promotes the Na-ion diffusion during the high-rate charge/discharge process. The poor rate performance and low specific capacity of the TiO_2 (1 : 1) electrode suggest that the highly compact structure with micropores also blocks the Na-ion diffusion during the charge/discharge process. The poorer Na-ion storage behaviour when compared to Li-ion storage for the TiO_2 (1 : 2) electrode reflects that the Na-ion cannot easily arrive at the centre of the interior dense area of TiO_2 (1 : 2) formed by several TiO_2 nanocrystals, which is quite different from the lithium ion transportation behaviour. Thus, the Na-ion diffusion length is crucial in determining the reaction speed of Na-ion storage.

Likewise, in order to clarify the kinetic behavior of the TiO_2 spheres in SIBs, CV curves of four TiO_2 electrodes at a scan rate of 0.1 mV s^{-1} in the range of 0.02–3.0 V were recorded (Fig. 6d).

 This journal is © The Royal Society of Chemistry 2017

Published on 14 November 2016. Downloaded on 04/04/2017 19:02:09.

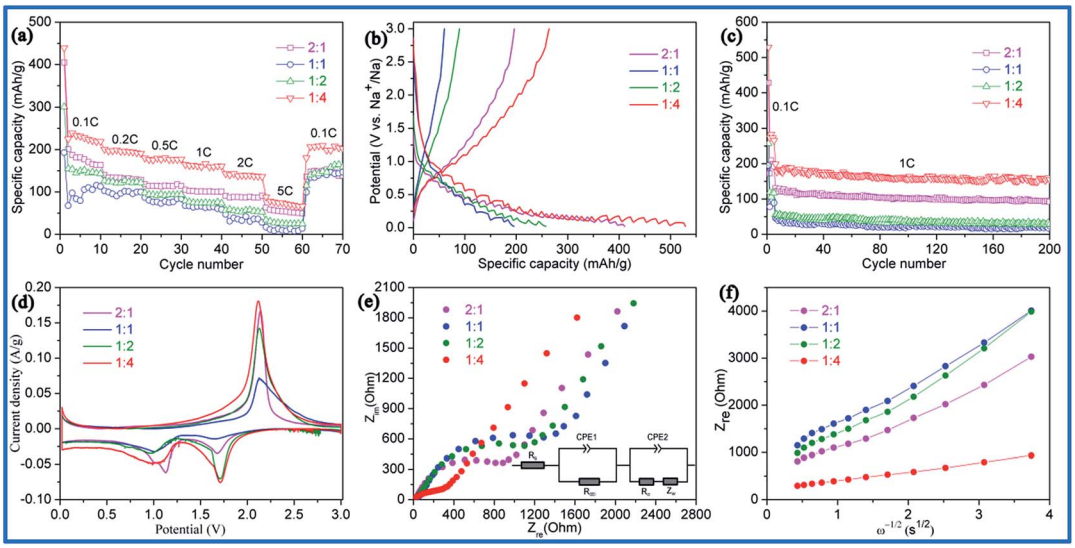

Fig. 6 Electrochemical characterization of the TiO_2 spheres for SIBs: (a) the rate and (c) cycling performances, (b) the first charge/discharge curves, (d) the cyclic voltammetry (CV) curves, (e) the Nyquist plots and (f) the plot of Z_{re} *versus* $\omega^{-1/2}$ in the low-frequency region.

The anodic peak located at 2.12 V may be attributed to the sodium extraction from the TiO_2 spheres. The much higher anodic peak current densities of the TiO_2 (2 : 1) and (1 : 4) electrodes signify their high kinetic properties and excellent high rate performance. The two cathodic peaks at 1.13 V and 1.70 V may be ascribed to the reaction of Na ions with the TiO_2 to form metallic titanium and Na ion insertion into the TiO_2 lattice.[17] Nyquist plots of the TiO_2 spheres show two partially overlapped and depressed semicircles at middle to high frequencies and a slope line at low frequencies, which are correlated with a solid electrolyte interface resistance (R_{SEI}), a charge transfer resistance (R_{ct}) and a Warburg diffusion process, respectively (Fig. 6e). The TiO_2 (1 : 4) electrode clearly exhibits a much lower R_{ct} (683 ohms) than the TiO_2 (2 : 1), TiO_2 (1 : 1) and TiO_2 (1 : 2) electrodes (1192, 1679, and 1902 ohms, respectively). In addition, the TiO_2 (1 : 4) electrode shows a much higher Warburg factor (σ_{Na}), suggesting a much larger Na ion diffusion coefficient (D_{Na}) than both the TiO_2 (2 : 1) and TiO_2 (1 : 1) electrodes (Fig. 6f). The much lower R_{ct} and larger D_{Na} of the TiO_2 (1 : 4) electrode lead to its excellent rate capability and cycling performance.

Based on the electrochemical characterizations of the different sized TiO_2 spheres for Li-ion and Na-ion batteries as noted above, it is clear that the pore distribution and the size of TiO_2 spheres profoundly influence their electrochemical properties. Meanwhile, the intrinsic properties of Li and Na-ions produce some difference in their (dis)charging process. Taken together, a schematic diagram is given to summarize the electrochemical reactions (Fig. 7). As shown in Fig. 7a, the small TiO_2 spheres with a size of 100 nm used as the anode for LIBs and SIBs exhibit excellent electrochemical performance due to their loose structure and shortened diffusion paths for Li-ions and Na-ions. However, with the increase in sphere size, the Li and Na-ions show obviously different storage properties with the same sized TiO_2 spheres (Fig. 7b). The Li-ion can easily transport to the centre of the interior dense area of TiO_2 (1 : 2) densely formed by several TiO_2 nanocrystals through micropores to react with TiO_2. In sharp contrast, the Na-ion almost cannot reach the centre of the dense area formed by micropores to react with the inner nanocrystals of TiO_2 spheres. Therefore, TiO_2 (1 : 2) shows poor Na-ion storage properties. The largely different Li-ion and Na-ion storage properties suggest that the Na-ion storage requires TiO_2 spheres with a loose structure in which TiO_2 nanocrystals cannot grow densely, while the Li-ion storage involves the porous structure of TiO_2 spheres with some interior area formed by TiO_2 nanocrystals densely.

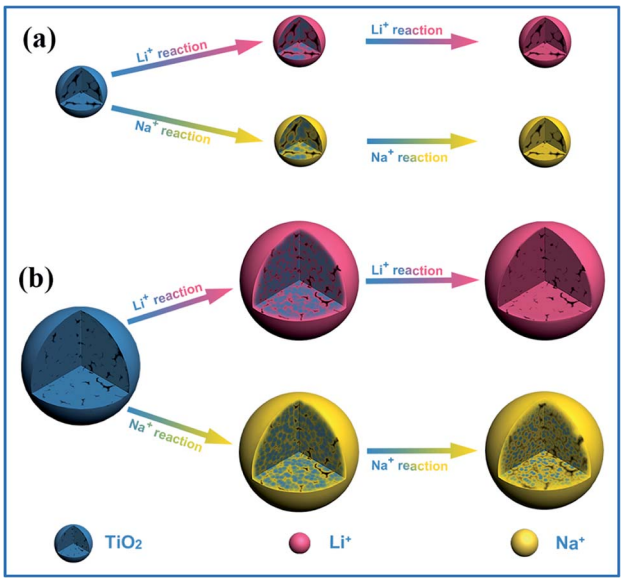

Fig. 7 Summary of the insertion of Li^+ and Na^+ in the (a) small and (b) large TiO_2 spheres.

Published on 14 November 2016. Downloaded on 04/04/2017 19:02:09.

Conclusions

We have developed a facile low-temperature hydrolysis strategy to craft size-controlled TiO_2 spheres with hierarchically porous architectures and high tap density. The dominant factors that control the Li-ion and Na-ion storage using TiO_2 spheres were scrutinized. It was found that the Li-ion and Na-ion storage and transportation required different pore distributions and sizes of TiO_2 spheres. In particular, the Li-ion storage and transportation relied heavily on the distribution and volume of micropores but not on the size of spheres. In contrast, the Na-ion storage and transportation demanded a loose structure with a high macropore volume for a shortened Na-ion diffusion length. The reduction in the size of TiO_2 spheres yielded a markedly improved performance in SIBs than in LIBs, due to the shortening of the Na-ion diffusion and penetration length. High tap-density TiO_2 spheres (1.06 g cm^{-3}) with excellent Li-ion and Na-ion storage properties were obtained with the Li-ion and Na-ion storage specific capacities at 1C of 189 mA h g^{-1} and 184 mA h g^{-1}, respectively. The TiO_2 spheres also demonstrated good rate and cycling performances. We envision that such a systematic investigation into the key factors that influence the Li-ion and Na-ion storage using high tap-density TiO_2 spheres as an electrode opens up an avenue to rationally design nanostructured TiO_2 for practical applications in Li-ion and Na-ion batteries.

Acknowledgements

This work was supported by the National Key Basic Research Program of China (2014CB932400), the National Natural Science Foundation of China (51232005), Shenzhen Basic Research Project (No. ZDSYS20140509172959981 and JCYJ20140417115840246), Youth research funds of the Graduate School at Shenzhen, Tsinghua University (QN20150002), Peng Cheng Scholar program (Z. L.) and Production-study-research cooperation project of Guangdong province (No. 2014B090901021) and Dongguan City (2015509119213).

Notes and references

1 X. Xin, X. Zhou, J. Wu, X. Yao and Z. Liu, *ACS Nano*, 2012, **6**, 11035.
2 G. Liu, H. G. Yang, J. Pan, Y. Q. Yang, G. Q. Lu and H.-M. Cheng, *Chem. Rev.*, 2014, **114**, 9559.
3 J. S. Chen, Y. L. Tan, C. M. Li, Y. L. Cheah, D. Luan, S. Madhavi, F. Y. Boey, L. A. Archer and X. W. Lou, *J. Am. Chem. Soc.*, 2010, **132**, 6124.
4 Z. Sun, J. H. Kim, Y. Zhao, F. Bijarbooneh, V. Malgras, Y. Lee, Y. M. Kang and S. X. Dou, *J. Am. Chem. Soc.*, 2011, **133**, 19314.
5 D. Wang, D. Choi, Z. Yang, V. V. Viswanathan, Z. Nie, C. Wang, Y. Song, J.-G. Zhang and J. Liu, *Chem. Mater.*, 2008, **20**, 3435.
6 Y. Lu, N. Zhang, Q. Zhao, J. Liang and J. Chen, *Nanoscale*, 2015, **7**, 2770.
7 M. Zhen, X. Guo, G. Gao, Z. Zhou and L. Liu, *Chem. Commun.*, 2014, **50**, 11915.
8 J. Ye, W. Liu, J. Cai, S. Chen, X. Zhao, H. Zhou and L. Qi, *J. Am. Chem. Soc.*, 2010, **133**, 933.
9 Y. Sun, L. Zhao, H. Pan, X. Lu, L. Gu, Y. S. Hu, H. Li, M. Armand, Y. Ikuhara, L. Chen and X. Huang, *Nat. Commun.*, 2013, **4**, 1870.
10 H. Liu, W. Li, D. Shen, D. Zhao and G. Wang, *J. Am. Chem. Soc.*, 2015, **137**, 13161.
11 B. Wang, H. Xin, X. Li, J. Cheng, G. Yang and F. Nie, *Sci. Rep.*, 2014, **4**, 3729.
12 G. Zhang, H. B. Wu, T. Song, U. Paik and X. W. Lou, *Angew. Chem., Int. Ed.*, 2014, **126**, 12590.
13 Y. Tang, Y. Zhang, J. Deng, J. Wei, H. Le Tam, B. K. Chandran, Z. Dong, Z. Chen and X. Chen, *Adv. Mater.*, 2014, **26**, 6111.
14 K. Saravanan, K. Ananthanarayanan and P. Balaya, *Energy Environ. Sci.*, 2010, **3**, 939.
15 L. Wu, D. Bresser, D. Buchholz, G. A. Giffin, C. R. Castro, A. Ochel and S. Passerini, *Adv. Energy Mater.*, 2015, **5**, 1401142.
16 S. Wu, C. Han, J. Iocozzia, M. Lu, R. Ge, R. Xu and Z. Lin, *Angew. Chem., Int. Ed.*, 2016, **55**, 7898.
17 D. Su, S. Dou and G. Wang, *Chem. Mater.*, 2015, **27**, 6022.
18 M. Søndergaard, K. Dalgaard, E. Bøjesen, K. Wonsyld, S. Dahl and B. Iversen, *J. Mater. Chem. A*, 2015, **3**, 18667.
19 D. Bresser, B. Oschmann, M. N. Tahir, F. Mueller, I. Lieberwirth, W. Tremel, R. Zentel and S. Passerini, *J. Electrochem. Soc.*, 2015, **162**, A3013.
20 Z. Bi, M. P. Paranthaman, P. A. Menchhofer, R. R. Dehoff, C. A. Bridges, M. Chi, B. Guo, X.-G. Sun and S. Dai, *J. Power Sources*, 2013, **222**, 461.
21 Y. Yang, X. Ji, M. Jing, H. Hou, Y. Zhu, L. Fang, X. Yang, Q. Chen and C. E. Banks, *J. Mater. Chem. A*, 2015, **3**, 5648.
22 Q. Tian, Y. Tian, Z. Zhang, C. Qiao, L. Yang and S.-I. Hirano, *J. Mater. Chem. A*, 2015, **3**, 10829.
23 H. Wang, D. Ma, X. Huang, Y. Huang and X. Zhang, *Sci. Rep.*, 2012, **2**, 701.
24 W. Li, F. Wang, Y. Liu, J. Wang, J. Yang, L. Zhang, A. A. Elzatahry, D. Al-Dahyan, Y. Xia and D. Zhao, *Nano Lett.*, 2015, **15**, 2186.
25 J. Jin, S.-Z. Huang, J. Shu, H.-E. Wang, Y. Li, Y. Yu, L.-H. Chen, B.-J. Wang and B.-L. Su, *Nano Energy*, 2015, **16**, 339.
26 S.-M. Oh, J.-Y. Hwang, C. S. Yoon, J. Lu, K. Amine, I. Belharouak and Y.-K. Sun, *ACS Appl. Mater. Interfaces*, 2014, **6**, 11295.
27 K. S. Novoselov, A. K. Geim, S. V. Morozov, D. Jiang, Y. Zhang, S. V. Dubonos, I. V. Grigorieva and A. A. Firsov, *Science*, 2004, **306**, 666.
28 S. Stankovich, D. A. Dikin, G. H. B. Dommett, K. M. Kohlhaas, E. J. Zimney, E. A. Stach, R. D. Piner, S. T. Nguyen and R. S. Ruoff, *Nature*, 2006, **442**, 282.
29 D. Wang, D. Choi, J. Li, Z. Yang, Z. Nie, R. Kou, D. Hu, C. Wang, L. V. Saraf, J. Zhang, I. A. Aksay and J. Liu, *ACS Nano*, 2009, **3**, 907.
30 Y.-B. He, M. Liu, Z.-L. Xu, B. Zhang, B. Li, F. Kang and J.-K. Kim, *Energy Technol.*, 2013, **1**, 668.

 This journal is © The Royal Society of Chemistry 2017

Published on 14 November 2016. Downloaded on 04/04/2017 19:02:09.

31 W. Lv, D.-M. Tang, Y.-B. He, C.-H. You, Z.-Q. Shi, X.-C. Chen, C.-M. Chen, P.-X. Hou, C. Liu and Q.-H. Yang, *ACS Nano*, 2009, **3**, 3730.
32 E. R. Camargo and M. Kakihana, *Chem. Mater.*, 2001, **13**, 1181.
33 P. Tengvall, T. P. Vikinge, I. Lundström and B. Liedberg, *J. Colloid Interface Sci.*, 1993, **160**, 10.
34 K. Tomita, V. Petrykin, M. Kobayashi, M. Shiro, M. Yoshimura and M. Kakihana, *Angew. Chem., Int. Ed.*, 2006, **45**, 2378.
35 S. Wang, Y. Ding, S. Xu, Y. Zhang, G. Li, L. Hu and S. Dai, *Chem.–Eur. J.*, 2014, **20**, 4916.
36 S. Wang, J. Xu, H. Ding, S. Pan, Y. Zhang and G. Li, *CrystEngComm*, 2012, **14**, 7672.
37 M. Giarola, A. Sanson, F. Monti, G. Mariotto, M. Bettinelli, A. Speghini and G. Salviulo, *Phys. Rev. B: Condens. Matter Mater. Phys.*, 2010, **81**, 174305.
38 R. P. Antony, A. Dasgupta, S. Mahana, D. Topwal, T. Mathews and S. Dhara, *J. Raman Spectrosc.*, 2015, **46**, 231.
39 D. C. Elias, R. R. Nair, T. M. G. Mohiuddin, S. V. Morozov, P. Blake, M. P. Halsall, A. C. Ferrari, D. W. Boukhvalov, M. I. Katsnelson, A. K. Geim and K. S. Novoselov, *Science*, 2009, **323**, 610.
40 A. C. Ferrari, J. C. Meyer, V. Scardaci, C. Casiraghi, M. Lazzeri, F. Mauri, S. Piscanec, D. Jiang, K. S. Novoselov, S. Roth and A. K. Geim, *Phys. Rev. Lett.*, 2006, **97**, 187401.
41 M. A. Pimenta, G. Dresselhaus, M. S. Dresselhaus, L. G. Cancado, A. Jorio and R. Saito, *Phys. Chem. Chem. Phys.*, 2007, **9**, 1276.
42 B. Jiang, C. Han, B. Li, Y. He and Z. Lin, *ACS Nano*, 2016, **10**, 2728.
43 S. Wu, R. Xu, M. Lu, R. Ge, J. Iocozzia, C. Han, B. Jiang and Z. Lin, *Adv. Energy Mater.*, 2015, **5**, 1500400.
44 H. Liu, Z. Bi, X. G. Sun, R. R. Unocic, M. P. Paranthaman, S. Dai and G. M. Brown, *Adv. Mater.*, 2011, **23**, 3450.
45 G. Hasegawa, Y. Ishihara, K. Kanamori, K. Miyazaki, Y. Yamada, K. Nakanishi and T. Abe, *Chem. Mater.*, 2011, **23**, 5208.
46 C. Han, D. Yang, Y. Yang, B. Jiang, Y. He, M. Wang, A.-Y. Song, Y.-B. He, B. Li and Z. Lin, *J. Mater. Chem. A*, 2015, **3**, 13340.
47 Z. Zhang, L. Zhang, W. Li, A. Yu and P. Wu, *ACS Appl. Mater. Interfaces*, 2015, **7**, 10395.
48 B. Qiu, M. Xing and J. Zhang, *J. Am. Chem. Soc.*, 2014, **136**, 5852.
49 X. Yan, Y. Li, F. Du, K. Zhu, Y. Zhang, A. Su, G. Chen and Y. Wei, *Nanoscale*, 2014, **6**, 4108.
50 J.-Y. Hwang, S.-T. Myung, J.-H. Lee, A. Abouimrane, I. Belharouak and Y.-K. Sun, *Nano Energy*, 2015, **16**, 218.
51 Y. Xu, M. Zhou, L. Wen, C. Wang, H. Zhao, Y. Mi, L. Liang, Q. Fu, M. Wu and Y. Lei, *Chem. Mater.*, 2015, **27**, 4274.
52 H. Usui, S. Yoshioka, K. Wasada, M. Shimizu and H. Sakaguchi, *ACS Appl. Mater. Interfaces*, 2015, **7**, 6567.
53 Y. Yeo, J.-W. Jung, K. Park and I.-D. Kim, *Sci. Rep.*, 2015, **5**, 13862.
54 C. Fu, T. Chen, W. Qin, T. Lu, Z. Sun, X. Xie and L. Pan, *Ionics*, 2015, **22**, 555.
55 J. Lee, Y.-M. Chen, Y. Zhu and B. D. Vogt, *ACS Appl. Mater. Interfaces*, 2014, **6**, 21011.